A Ring Gyroscope With On-Chip Capacitive Stress Compensation

Baha Erim Uzunoglu, Derin Erkan, and Erdinc Tatar, *Member, IEEE*

Abstract—We present long-term stress compensation results for a 3.2mm diameter ring gyroscope integrated with 16 capacitive stress sensors for the first time in this work. A bridge-type capacitive sensor is preferred due to its compact size and temperature insensitivity for on-chip stress measurements. The ring design enables a high level of integration and stress sensor-gyroscope output correlation. We first demonstrate the stress sensor operation on a stress test-bed. The drift test for sixteen days at mismatched mode and the drift test for eight days at matched mode in room temperature reveal that the stress compensation can eliminate the gyroscope drift. The stability of the stress compensated gyroscope output can reach 0.008°/h in mismatched mode and 0.003°/h in matched mode at an averaging time of two days with no signs of long-term drift. High gyroscope stability is achieved with a partial least-squares fitting algorithm; however, we believe that stress and gyroscope output relation might be linear time-variant with possible nonlinear and hysteresis effects. Analysis of the drive and sense mode frequencies shows that only temperature cannot explain the frequency variations, and the inclusion of stress can comprehensively describe the frequency changes.   [2022-0108]

Index Terms—MEMS inertial sensors, ring gyroscope, stress sensor, drift, stress compensation.

I. INTRODUCTION

MEMS Gyroscopes offer low power, low-cost, high accuracy rotation rate measurement in a compact footprint, meeting the increasing demand in navigation, robotics, automotive, and consumer industries. The Hemispherical Resonator Gyroscope (HRG) is one of the main inspiration sources for MEMS gyroscopes [1]. HRG's high performance is a product of the symmetric hemispherical shell with the matched electrodes. Inspired by the HRG, both 2-D and 3-D circular gyroscope structures have gained attention in recent years, [2], [3], [4], [5], [6], [7]. A circular topology leads to degenerate gyroscope modes that frequency match and

track each other naturally against environmental stress and temperature variations. The inherent matching between the modes improves the long-term stability of circular gyroscopes.

Disc Resonator Gyroscopes (DRGs) that consist of multiple nested rings represent a significant part of circular gyroscope designs in the literature. DRGs with high stability have been demonstrated in the recent years, for example Boeing's Disc Resonator Gyroscope achieved 0.012 °/hr bias instability [3]. Xu *et al.* reached a similar bias instability level of 0.015°/hr with a honeycomb DRG [4]. Another design approach to realize a circular gyroscope is utilizing a single ring and suspension [5], and commercial ring gyroscopes with a bias instability of less than 0.03°/h are available [6]. In addition to in-plane circular gyroscopes, a miniature version of the HRG accomplished a bias instability of 0.0014°/hr with a 3D fused-silica micro precision shell integrating gyroscope [7]. It is noteworthy to mention that high performance gyroscopes have also been illustrated with rectangular devices. Gadola *et al.* showed 0.02°/h bias instability in a 1.3mm^2 area with nano-piezoresistive sensing technology [8]. Stability of 0.01 °/hr has been demonstrated by Thales [9] and Honeywell [10] with tuning fork structures. Although the performance of the MEMS gyroscopes has reached near navigation grade, the long-term drift still remains as a major performance-limiting factor. As the main novelty, this study focuses on the suppression of the long-term gyroscope drift with stress compensation rather than enhancing the gyroscope noise performance to lower the bias instability.

Long-term gyroscope drift, characterized by the Rate Ramp and Rate Random walk in the Allan Variance test [11], manifests itself as increased standard deviation for long averaging intervals [4], [7]. Multiple days to weeks-long tests are required to observe the long-term drift effects clearly. Although the exact source of long-term drift still remains undiscovered, environmental stress and temperature variations are thought to be the primary source [12]. A widely used drift suppression method is temperature calibration. Most of the high-end commercial gyroscopes and IMUs are temperature compensated at the factory [13]. Temperature is a major source of the gyroscope drift; however, temperature calibration does not eliminate drift entirely. In [14] an ovenized crystal oscillator (OCXO) has been integrated with the Boeing DRG for temperature sensing, and the gyroscope is ovenized within 1mK. Yet, the residual long-term drift was still present. We believe temperature sensing is necessary but not sufficient to eliminate the gyroscope drift. In addition to temperature, Ge *et al.* excited the n = 2 and n = 3 modes of a DRG
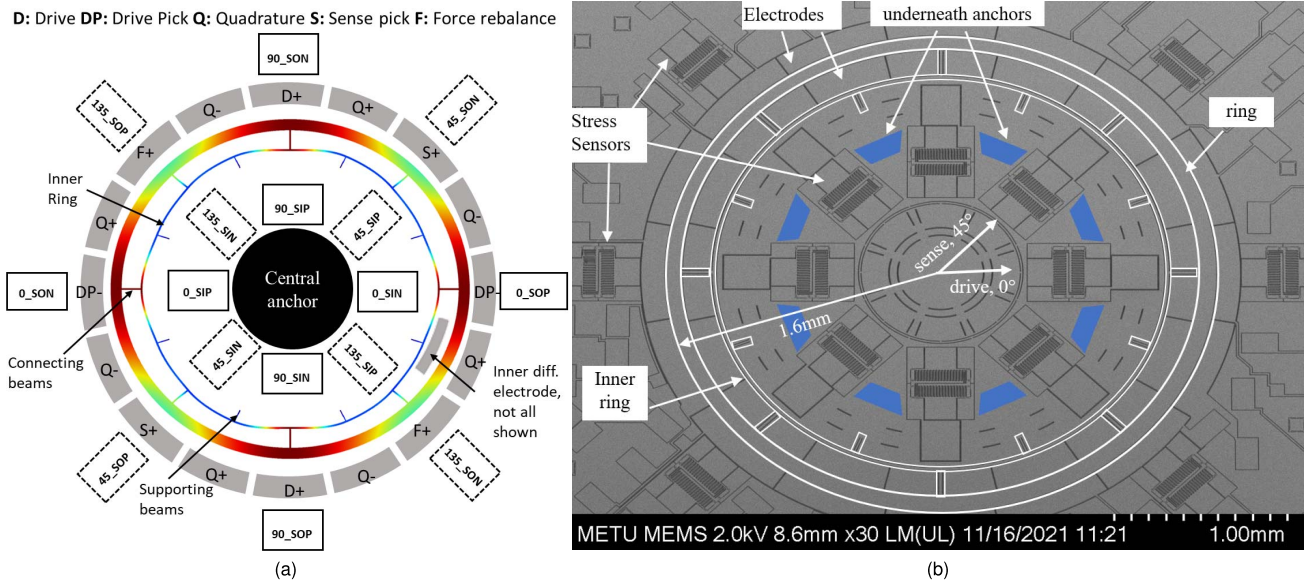
Fig. 1. The gyroscope design summary (a), and the SEM image of the gyroscope with the integrated stress sensors (b).

simultaneously and used the n = 3 mode to compensate the long-term drift of the n = 2 wine glass mode [15]. The long-term drift improved as a result, but was not completely removed.

The effect of temperature change on long-term drift is an extensively researched topic while the impact of stress is relatively unknown. In [16], predetermined input stress obtained from Finite Element Analysis (FEA) was applied to a gyroscope and the resulting change in the gyroscope output was studied with a circuit-based simulation. Zhang *et al.* provided an FEA simulation model for the sensor to package interaction to decrease the output signal offset [17]. Even though these particular studies are helpful in understanding the consequences of the induced stress upon the device, stress can vary depending on the fabrication process and the type of die to package attachment [18]. From these findings, it can be argued that on-chip stress sensing is essential for long-term drift suppression.

On-chip stress compensation with piezoresistive stress sensors has been shown to improve the long-term stability of MEMS gyroscopes [19]. The piezoresistive sensor outputs can be read in a simple Wheatstone bridge configuration. Piezoresistive stress sensors are widely utilized in pressure sensors [20], and piezoresistive stress sensor arrays were used to characterize IC packaging stress [21]. Compact piezoresistive stress sensors can be built in an IC process with high resistance layers; however, piezoresistors occupy a large real estate in inertial MEMS applications. MEMS inertial sensors are fabricated on thick ($> 10\mu m$), highly conductive silicon that results in long piezoresistors for a moderate resistance. Piezoresistance of silicon is also temperature dependent requiring calibration [22]. Alternatively, capacitive stress sensors can be designed [23], [24]. Capacitive stress sensors convert the anchor displacements into capacitance changes with mechanical amplification. Capacitive stress sensors can be made compact, consume low power, and do not have temperature dependence. The major drawback of the capacitive stress

sensors compared with the piezoresistive sensors is the more complex readout circuit, which requires demodulation at the clock frequency. But, the demodulation is similar to the gyroscope readout and thus not difficult to implement. Multiple compact on-chip stress sensors are needed for high-resolution stress compensation, and a modified bridge-type capacitive stress sensor [25] was used in our design.

In this work, we integrated a 3.2mm diameter ring gyroscope with 16 capacitive stress sensors. We provide the mechanical stress test measurements, the long-term drift compensation results with stress for mismatched and matched mode operation, and the drive and sense frequency analysis with stress for the first time to our knowledge. The device interacts with the external environment through the anchors. A circular gyroscope structure with a central support anchor and electrodes on the periphery enables the placement of stress sensors in the close vicinity of the anchors. The tight integration leads to accurate stress assessment and compensation. Since the anchors are distributed all over the device in a rectangular gyroscope design [26], the stress sensors are located outside the device. Average stress is monitored as a result. If, for example, there is a stress gradient within the device, the average stress measurement might fail to accurately capture the stress information.

This paper is organized as follows: Section II explains the gyroscope and capacitive stress sensor design, Section III provides details about the test setup and the readout of the gyroscope and integrated stress sensors, and Section IV reports the external stress tests and extensive long-term test results along with the drive and sense frequencies and shows the effectiveness of the stress compensation. Finally, Section V concludes the paper.

II. GYROSCOPE AND STRESS SENSOR DESIGN

Figure 1.a presents the high-level picture of our design approach, and Figure 1.b provides the SEM image of
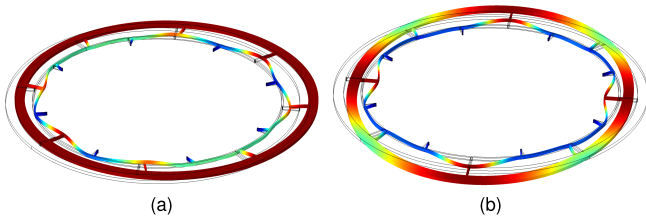
Fig. 2. n = 1 acceleration-sensitive mode with f_{res} = 47.3kHz (a), and n = 2 wineglass mode with f_{res} = 63.2kHz (b).

our gyroscope with the integrated capacitive stress sensors. We designed a Vibrating Ring Gyroscope (VRG) that is suspended by an inner ring and additional support and connection beams. The capacitive differential electrodes are located on the outer periphery of the ring and between the inner suspension ring and the main ring. We picked a ring structure over a DRG due to its simpler design. The sparse structure of the ring enabled us to place stress sensors on the inside and outside of the gyroscope. The stress sensors are located every 45° with a total of 8 inside and 8 outside sensors. The stress sensors are named based on their location and polarity. We use O for outer, I for inner; and P for the positive polarity, N for negative polarity. 45_SIP means, the stress sensor is located at 45° at the inside of the ring and has positive polarity.

The stress of the mechanical support anchors and the electrodes can be monitored accurately thanks to tight integration. At any given material cross-section, stress is a tensor with normal and shear components. Only specific stress components can be measured due to finite space, so we monitor the in-plane stress orthogonal to the capacitive gaps. This configuration gives us an indication of the parallel plate capacitance gap changes and the longitudinal stress on the supporting and connecting beams.

The VRG has an outer radius of 1.6mm with 100μm ring width and 35μm thickness, and operates in n = 2 wine-glass mode. A detailed analytical analysis of the ring with process imperfections can be found in [27]. The natural frequency of the ring is 43.8kHz, excluding the suspension. The final designed resonance frequency is 63.2kHz. The choice of a larger resonance frequency (f_{res}) compared to [3], [4], [5], [6], [7] which has f_{res} < 15kHz has two main reasons: (i) To be compact in size, a smaller diameter results in higher f_{res} since $f_{res} \sim 1/R^2$ [28]. (ii) To reduce the in-plane acceleration sensitivity. Figure 2 shows the mode shapes of the acceleration-sensitive mode at 47.3kHz (Fig.2.a) and the n = 2 wine glass mode of the ring at 63.2kHz (Fig.2.b). The acceleration-sensitive mode is the rigid body mode (n = 1 mode), where the spring constant is set by the internal suspension, and the modal mass is the entire ring. For n = 2 mode, the effective modal mass is less than the ring mass, and the effective stiffness is the sum of the ring and the internal suspension stiffness. So, the n = 2 mode has a higher spring constant and lower effective mass compared to the n = 1 mode. As an inherent feature of our ring gyroscope design, the n = 1 mode frequency is lower than the n = 2 mode frequency. We stiffened up the internal suspension to increase the n = 1 mode frequency, which

resulted in 47.3kHz n = 1 mode frequency and 63.2kHz n = 2 wineglass mode frequency. Differential reading cancels the in-plane acceleration sensitivity effects at the output to the first order; however, the gap mismatches across the device lead to a non-zero acceleration sensitivity [29]. A higher n = 1 mode frequency reduces the overall acceleration sensitivity ($\sim 1/\omega_1^2$). Another approach to suppress the acceleration sensitivity for a circular gyroscope is designing MHz frequency Bulk Acoustic Wave Devices [30], which requires nm gaps to drive the stiff mechanical structure. Mode ordering studies similar to [31] can enable a higher n = 1 mode frequency compared to the n = 2 mode. The focus would be substantially increasing common mode stiffness.

We outsourced the fabrication of the devices. The devices are fabricated in a wafer-level vacuum packaged silicon-on-glass process with vertical feed-throughs [32]. The device layer is highly conductive, ⟨111⟩ 35μm thick silicon. The VRG electrodes can be seen in Figure 1. We use the 0° mode as the drive and 45° mode as the sense mode. The quadrature cancellation electrodes are located between the drive and sense electrodes. The device is designed to be perfectly symmetric; however, fabrication imperfections can result in slight frequency mismatches. The maximum frequency split we measured is 65Hz based on 12 tested devices in probe. We have dedicated frequency tuning electrodes to compensate for the frequency mismatches due to fabrication tolerances and material anisotropy. Our active MEMS area including all the stress sensors is 4.5 × 4.5mm. The final die size is 7.9 × 7.9mm to meet the specifications of the manufacturing process, and the die size is not optimized in this work.

The design of the capacitive stress sensor is based on a cm-sized macro-scale bridge-type displacement amplifier [25]. We scaled down the cm-sized device as a strain amplifying capacitive sensor. Figure 3.a illustrates the SEM image of the fabricated stress sensor with the equivalent electrical circuit, and Figure 3.b presents the FEA image showing the operation principle. The unbalanced bridge connection to the anchors and to the movable structure amplifies the anchor displacements (stress) in orthogonal directions. The anchor displacements in the x-direction are converted into y displacement, which is then translated into capacitive changes as shown in Figure 3.b. The mechanical gain of the device is $1/\tan(\alpha)$ and set by the unbalance in the bridge. The gain is set to 6.5 in our design, and the overall size of the device is 480μm × 386μm. The resonance frequency of the stress sensor is far away from the gyroscope operation frequency at 304kHz. The stress sensor operates at DC, and the applied 10kHz differential clock signals (V_{mod+}/V_{mod-}) modulate the stress signal away from the 1/f noise corner of the electronics. The readout of the stress sensor is a transimpedance amplifier followed by a demodulator at 10kHz, almost identical to the gyroscope readout. Operating the gyroscope and the stress sensor at different frequencies minimizes the undesired coupling between them.

III. TEST SETUP

Figure 4.a shows the high-level schematic of our test setup. The PCB includes the signal conditioning electronics
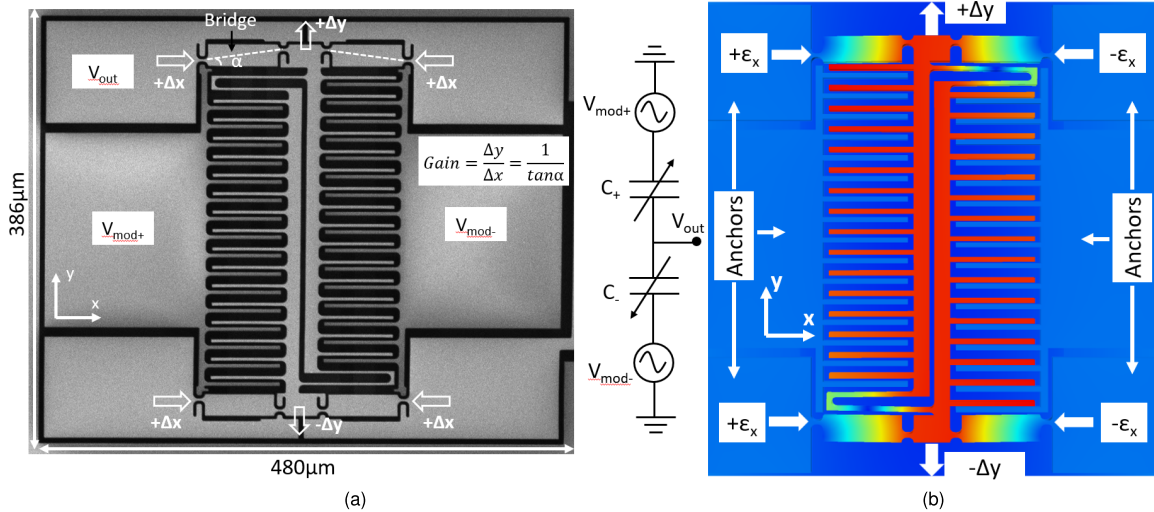
Fig. 3. The stress sensor SEM image and the electrical equivalent circuit (a), and the FEA image showing the operation principle (b).
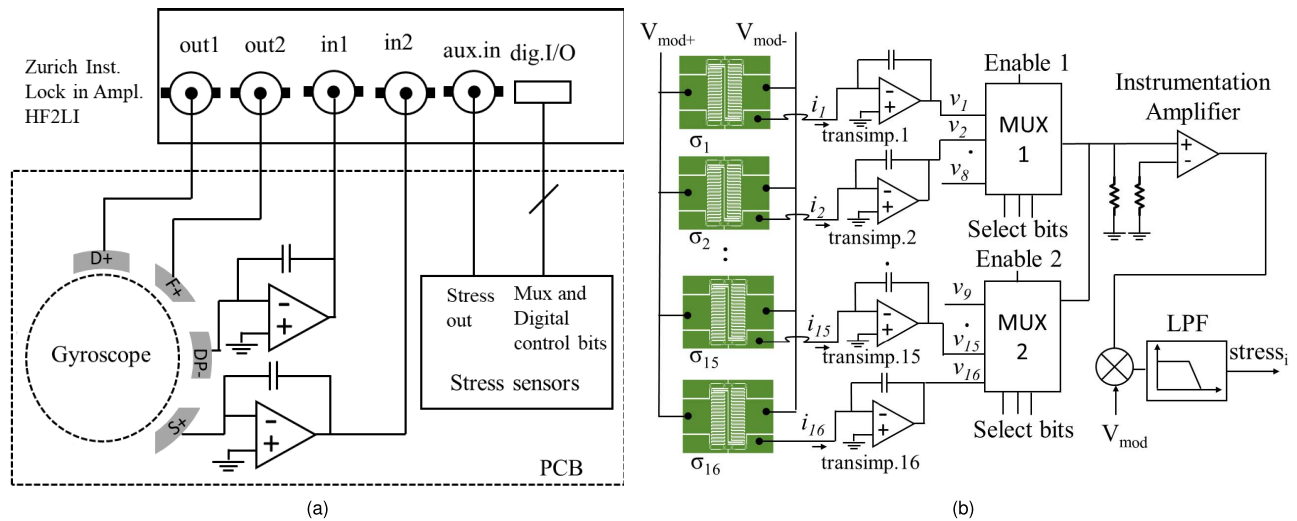

Fig. 4. High level schematic of our test setup (a), and the stress sensor signal chain (b).

for the gyroscope and stress sensors, multiplexers, hardware demodulator, and voltage regulators. We use Zurich Instruments HF2LI [33] to control the gyroscope and the stress sensors and to record the data. The gyroscope control includes demodulation, PLL to lock-in to the drive resonance frequency, closed-loop drive amplitude control, and quadrature cancellation for the sense mode. Although Force Rebalance could be implemented, we operate the gyroscope sense mode open-loop in this study. The two channels of the HF2LI are dedicated to the drive and sense modes of the gyroscope. The stress sensor outputs are modulated to 10kHz and are demodulated in hardware with an analog multiplier (AD633) followed by an analog low-pass filter (LPF). The demodulated data is recorded through the Auxiliary Input of the HF2LI.

There are 16 stress sensors in our design. Employing 16 demodulation channels for continuous data capture would not be efficient in terms of power and readout area. We note that the die stress is a slowly changing physical variable with a time constant probably in the order of minutes to

hours. Therefore, a high bandwidth stress measurement is not necessary. We designed a multiplexed readout system as shown in Figure 4.b by considering the large time constant of stress. All the stress sensor outputs are first preamplified and then multiplexed. We used two 8×1 multiplexers. The output of the multiplexer is amplified by an instrumentation amplifier (AD8295) and then hardware demodulated. We read one stress sensor output at a given time. The digital control signals for the multiplexers are generated by the digital I/Os of the HF2LI. During our characterization, we noticed that while the stress output switches from one multiplexer to the other, the input of the instrumentation amplifier goes to high Z. The instrumentation amplifier rails due to the DC input offset current. Adding high resistances to the input of the instrumentation amplifier provides a DC current path without loading the previous stages and solves the saturation problem.

Figure 5.a shows the picture of our test setup. The main PCB is connected to an interface board where all the external and power connections are established. In addition to HF2LI,
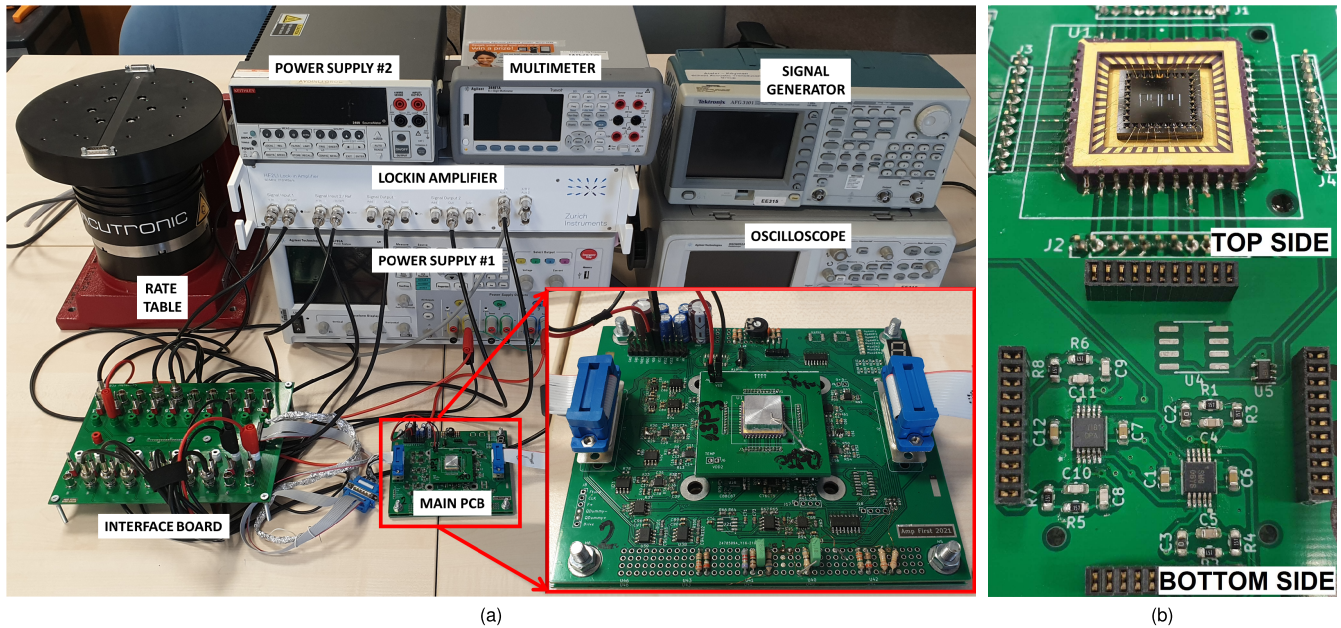
Fig. 5.   Photo of the test setup (a), and the daughter board that houses the gyroscope and preamplifiers (b).
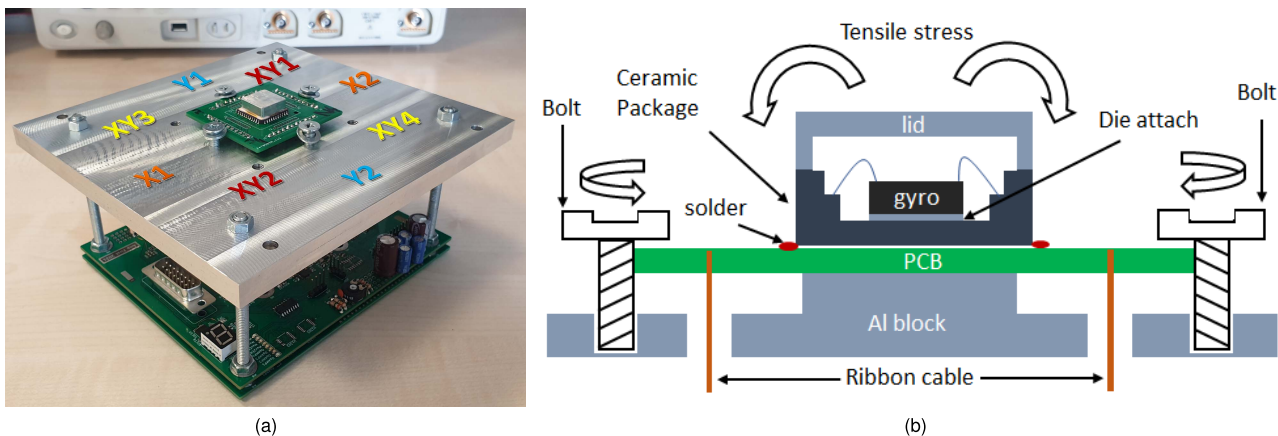

Fig. 6.   Photo of the aluminum stress test-bed (a), and the image showing the external stress test concept (b).

we use a digital multimeter to record the PCB temperature. The gyroscope chip is mounted to a 44pin ceramic LCC. We then solder the ceramic package to a daughter board as illustrated in Figure 5.b. The daughter board acts as a socket and is plugged into the main PCB. The overall MEMS die height including the wirebonds is higher than the LCC depth. So, we custom-machined an Aluminum cap to accommodate the extra height. Aluminum cap could be optimized, currently its height is much larger than the required height. In order to minimize the parasitic capacitance on the pick-offs, the gyroscope front end amplifiers are mounted on the backside of the daughter board. Since there are 16 stress sensor front ends, they are located on the main PCB. We used low noise OPAMPs (Texas Instruments, OPA2320) for both the gyroscope and stress sensor pre-amplifiers. Our tests are controlled by a Python code. The gyroscope and temperature output are recorded continuously, and the stress sensor outputs are switched every 1.3 seconds.

IV. TEST RESULTS

The strength of the long-term drift compensation is determined by the performance of the stress sensors and the gyroscope. Towards that end, we tested the accuracy of the on-chip stress sensors by applying stress in different directions on an aluminum test-bed. Next, we performed long-term gyroscope drift tests with on-chip stress sensors at room temperature for mode mismatched and mode matched conditions. Finally, we tested and analyzed the drive and sense frequencies over time to observe the effects of stress and temperature. We present the details of the test results in the below subsections.

A. External Stress Test Results

We designed a stress test-bed to test the functionality of the stress sensors. Figure 6.a shows the picture of our stress test setup. The daughter board housing the gyroscope is located
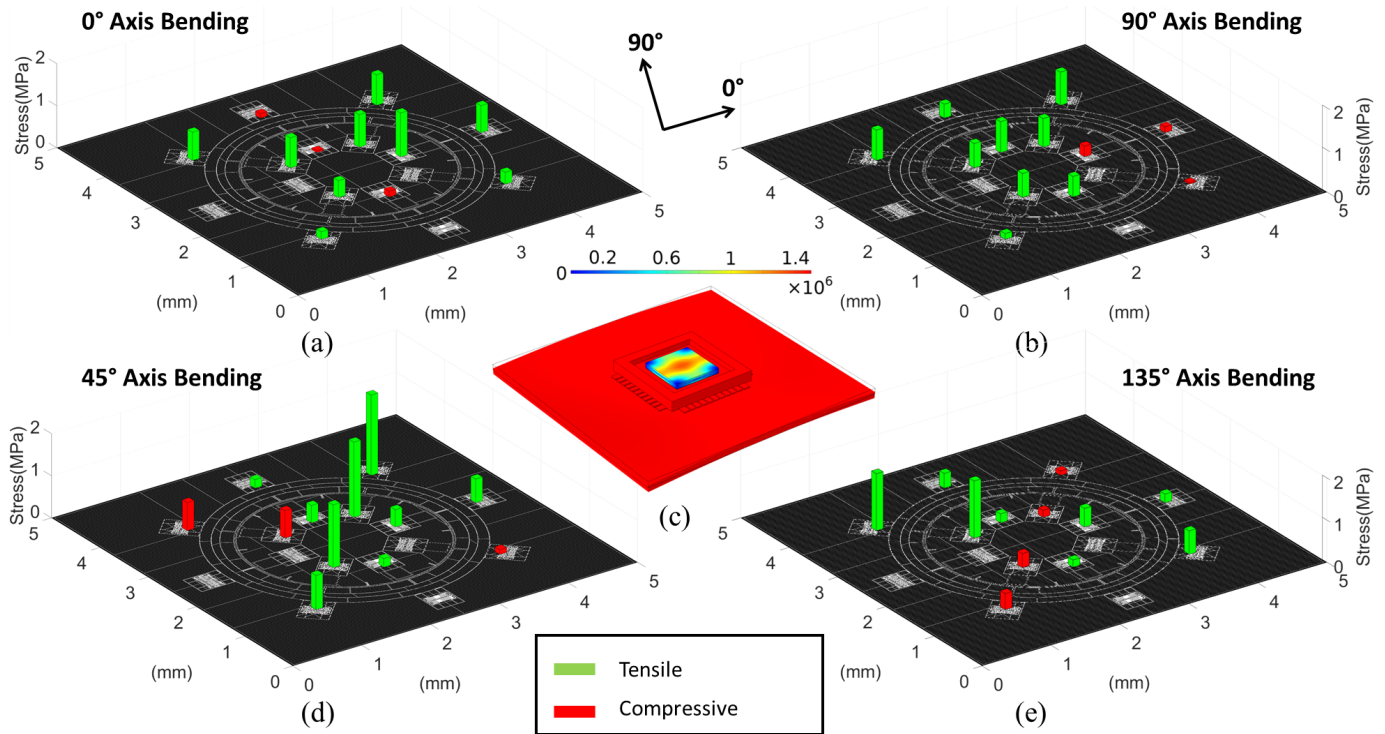
Fig. 7.   Stress testbed results: Normal stress bending on X1-X2 axis (a), Normal stress bending on Y1-Y2 axis (b), Shear stress bending on XY1-XY2 axis (d), Shear stress bending on XY3-XY4 axis (e), and the FEA analysis of the daughter PCB on X1-X2 axis (c).

on an elevated aluminum platform. Flexible ribbon cables connect the gyroscope and stress sensor signals to the main PCB. Selectively turning the bolts on the aluminum platform generates normal stress in x and y directions (σ_x, σ_y), and shear stress (σ_{xy}) on the MEMS die. Figure 6.b presents the concept of our stress test-bed. Since the bottom of the daughter board should be flat for uniform stress application, we moved the gyroscope pre-amplifiers to the main PCB for this test. The stress is applied to the MEMS die only with this setup, and the electronics remain stress free. We performed the following 4 different stress tests:

σ_x test by tightening the bolts X1 and X2,
σ_y test by tightening the bolts Y1 and Y2,
σ_{xy} along 45° test by tightening the bolts XY1 and XY2,
σ_{xy} along 135° test by tightening the bolts XY3 and XY4.

The bolts are labeled in Figure 6.a. Tightening the bolts generates tensile stress along the tightening direction. Figure 7 presents the measured stress results. We plotted the stress difference between the bolt tightened and bolt released cases. We provide data from 12 stress sensors, there are 4 non-functional stress sensors due to connectivity issues. The bars are placed on top of the stress sensor locations on the gyroscope. The green and red colors represent tensile and compressive stress, respectively. We use a soft die attach (ThermoBond 3508, United Adhesives) with a Young's Modulus of ∼6MPa. So, the maximum measured stress is relatively on the low side, 1-2MPa. The stress distribution is more intuitive when we look into bending along 45° and 135° stress tests. Bending the die along 45° generates tensile stress along 45° and compressive stress along 135° due to Poisson's ratio. We clearly observe diagonal tensile and compressive stress in the Figure 7.d-e

consistent with the expectations. Similarly in the 0° bend test, stress sensors on the 0° axis measure tensile, and stress sensors on the 90° axis measure compressive stress. The exact opposite results are obtained in the 90° axis bend test. In general, uniform tensile stress is observed in the 0° and 90° bend tests. The aluminum square underneath the daughter board act as the anchor for the stress tests. In 45° and 135° bending tests, the corner of the square becomes a pivot point. So, bending along a point creates concentrated stress. However, in 0° and 90° tests the side of the square becomes the pivot and bending along a line creates a more uniform stress.

FEA of our test-bed along 0° bending also shows an almost uniform tensile stress in the order of 1-2MPa as shown in Figure 7.c. Note that we limited the maximum shown stress to improve the visibility of the die stress in FEA. Since it is not straightforward to apply a known stress to obtain the sensitivity of the stress sensors, we used calculated sensitivity based on FEA for the mechanical gain and SEM measurements for the capacitive gaps. The discrepancies with respect to ideal stress distribution can be attributed to the non-idealities in the system; such as non-symmetric die location and stress application, and non-uniform die-attach thickness. Overall, we think the stress test results verify the functionality of our stress sensors.

B. Drift Test Results in Mismatched Mode

Different gyroscopes are employed for the stress and drift tests. Table I shows the parameters for the gyroscope utilized in the drift tests with 16 functional stress sensors. The gyroscope drive frequency of 57.355kHz is lower than the

TABLE I
VRG PARAMETERES

Parameter	Value
Drive Frequency	57,355 Hertz
As Born Sense Frequency(Ftune=0V)	57,361 Hertz
Mismatched Sense Frequency(Ftune=40V)	57,415 Hertz
Proof Mass High Voltage	50V
Quality Factor	30,000
Effective Proof Mass	0.5115 e-07 kg
Angular Gain	0.3898

63.2kHz design value. Based on our modeling and SEM measurements, there is 1μm over-etch in the internal suspension. We tested the long-term drift of the gyroscope under frequency mismatched and frequency matched conditions. As born frequency mismatch between the drive and sense modes is 6Hz. We applied 40V to the frequency tuning electrodes to generate a mismatch between the modes. $f_{sense} > f_{drive}$ and $f_{sense} - f_{drive} = 60$Hz for the mismatched case. We apply 50V to the proof mass. So, increasing the sense mode frequency tuning voltage from 0 to 40V reduces the softening and leads to a higher frequency. We estimate the drive displacement to be 1μm in a 3.6μm gap. We ran our tests at room temperature without any temperature control. The temperature is measured with a PTAT (LMT87) on the PCB. Since the room temperature changes with a time constant in the order of hours, the gyroscope and PCB temperatures are assumed to be the same.

During the tests, the gyroscope and temperature outputs are recorded continuously; however, the stress sensor outputs are multiplexed. We linearly up-sample the stress sensor outputs to match the sampling rates for the fitting algorithm. As expected, we observed a large stress time constant (20-30mins), and the resolution of the stress sensors is not as good as the gyroscope output. We ran a 2-hour moving average on the stress sensors to suppress the white noise and improve the fitting quality. After subtracting the DC offsets, we find the relation between the gyroscope zero rate output (ZRO) and 16 stress sensors and temperature with the least-squares fitting algorithm. We assume that the long-term drift of the gyroscope output can be expressed as a linear function of stress and temperature. We are aware that the least-squares method is one of the simple fitting algorithms and might not be optimal for our application. But, least-squares method is a convenient starting point to demonstrate the concept before further iterations. The least-squares formulation is shown in Equations (1) and (2) where y ($m*1$) represents the time domain gyroscope output with m number of samples, X ($m*n$) represents the time domain up-sampled stress and temperature sensor outputs with a total number of n sensors. We calculate the coefficient matrix b, and then find e as the gyroscope ZRO, which are the residuals of the fitting.

$$y = Xb, \quad b = (X^T X)^{-1} X^T y \qquad (1)$$
$$e = y - Xb = y - X(X^T X)^{-1} X^T y \qquad (2)$$

We performed the tests with the quadrature loop open and closed. When the quadrature loop is open, we tune the quadrature before starting the test, and leave the quadrature

voltage as is during the experiment. We observed a strong correlation between the quadrature and stress, even though demodulation phase was adjusted. The gyroscope stability deteriorated as a result. Coefficient of thermal expansion (CTE) differences of the materials (die attach, package, solder, PCB) might induce non-repeatable stress with room temperature fluctuations. The uncompensated quadrature signal couples to the ZRO through the phase errors in the system. We ran our subsequent tests with the quadrature loop closed to minimize the original drift.

Figure 8 presents the time domain plots for the 16 stress sensors, temperature, and original and compensated gyroscope ZRO for the 16 day drift test under mismatched operation. The stress sensor locations are shown in Figure 1.a. The stress sensors generate positive output for tensile stress. The distributed gyroscope stress along with the gyroscope ZRO is presented for the first time for a circular gyroscope to our knowledge. The temperature fluctuates about 1°C during the day and night due to the heating system of the building. The overall temperature increased about 3°C over 16 days because of the general weather conditions in our region. The effect of temperature variations on stress measurements can be observed, but the temperature-stress correlation is not direct. For most of the stress sensors there is a linear increase. The maximum stress variation over 16 days is <1MPa. Increasing temperature causes tensile stress. The gyroscope materials (glass and Si) have lower CTE compared to the epoxy, ceramic, solder, and PCB. We think that as the temperature rises, surrounding material wants to expand more resulting in a tensile stress on the gyroscope. The stress measurements show that the on-chip stress is not uniform, and distributed stress measurement is necessary to capture an accurate assessment of the stress distribution. The day and night temperature fluctuations are not very clear on the gyroscope output. The closed-loop quadrature control is essential, the uncompensated gyroscope bias instability improved by 2.3X compared to the quadrature loop open case, similar to [34]. Even though suppressed, there is still a clear drift at the gyroscope output.

Figure 9 shows the Allan Variance plots for different compensation cases for the 16 day long drift test. The original uncompensated gyroscope output has a bias instability of 0.7°/h and Angle Random Walk (ARW) of $0.233°/\sqrt{h}$. The ARW performance is limited by the parasitic capacitance at the sense mode output. There is a small bump around 20s. Reading the 16 stress sensor outputs takes 20s, and an undesired coupling occurs between the stress sensors and the gyroscope when the multiplexers switch between the stress sensors. The multiplexer transitions between the stress sensor outputs very quickly generating a pulse. The immediate transition and the shared front-end power supplies can be the source of the undesired coupling. Only temperature compensation does not improve the performance significantly. Temperature and stress compensation improves the performance slightly better at the very long time scales. It is not plotted, but there is no difference between stress compensation and stress and temperature compensation since the stress data already contains the temperature.
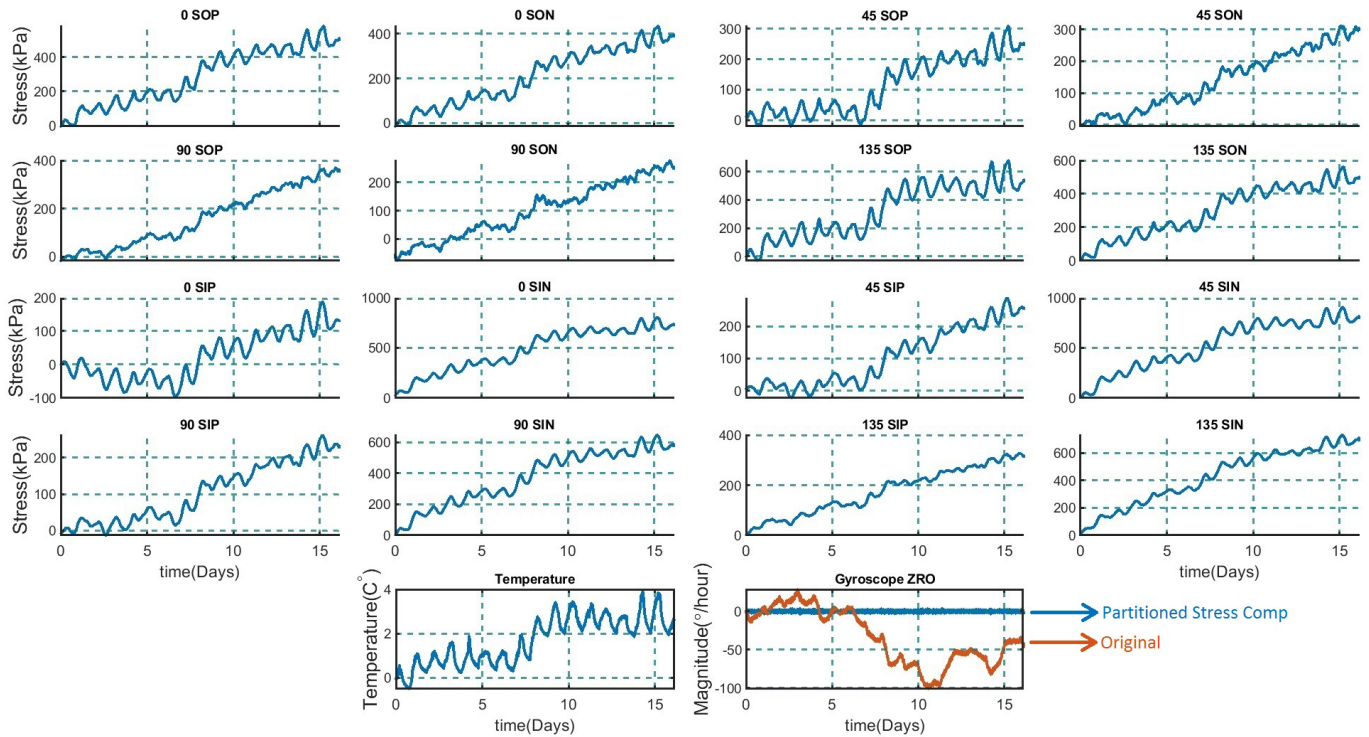
Fig. 8. The time domain plot of the 16 stress sensors, the temperature sensor and ZRO of the gyroscope in mismatched frequency operation for 16 days. The variations over time are plotted, refer to Fig.1.a for stress sensor locations.

We have run Allan Variance analysis on different time periods of the data and noticed that we obtain significant improvement for shorter time periods. For example, running the least-squares algorithm for the first day or few days eradicates the long-term drift completely, and we observe only ARW slope. Or if we take 1 day chunks of data and run our algorithm, the long-term drift is totally eliminated. There is a consistent correlation between the gyroscope drift and stress sensor outputs, but the correlation coefficients change over time. In a day or few days, the change in the coefficients cannot be noticed, but the coefficient variation is visible for longer time periods. We hypothesize that the stress-gyroscope output relation might be linear time-variant or nonlinear with hysteresis effects. Our least-squares algorithm is a simple linear fit, so a linear time-invariant fit to a time-variant or a nonlinear curve would work in small regions, but would not work on the entire data set. In order to show the effectiveness of the least-squares fitting in shorter time periods, we divided our data into 12 hour data sets, and computed the individual compensation coefficients for each 12 hours. We then assembled the 12-hour data sets and performed the Allan Variance analysis on the 16 day data. The results are shown as "Partitioned Stress Comp" in Figure 9. We achieve 0.008 °/h stability at 2 days of averaging with no signs of long-term drift. Applying the same 12-hour partitioned compensation just using the temperature data provides 100X worse results. Temperature is unable to fully capture the drift behavior even in short periods, but stress can successfully characterize the drift. Compensating the data every 12 hours is not practical, but it shows that the gyroscope ZRO is consistently related with the stress. Based on these findings, we can conclude that
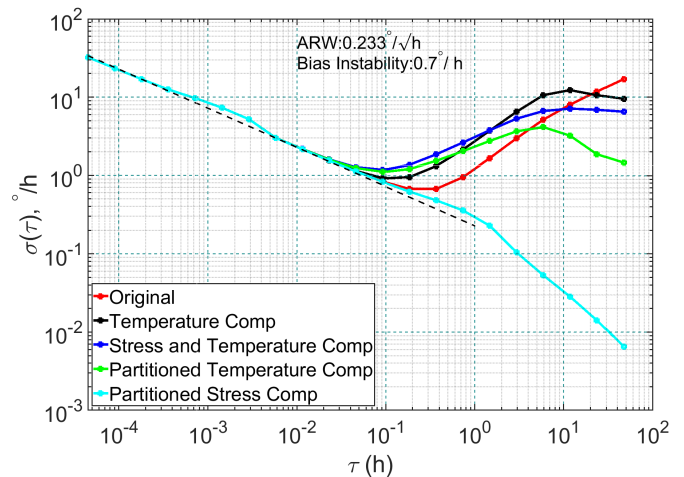

Fig. 9. The Allan deviation plots of the gyroscope output in mismatched operation for 16 days for various compensation cases.

the least-squares fitting is not the optimal method for stress compensation. As the next stage of our research, we will look into more advanced fitting algorithms. Since we have a large amount of data, machine learning algorithms might provide a solution to our problem. The bump around 1 hour in the partitioned stress compensated Allan Deviation plot results from the 2 hour moving average filter we used in the stress sensor outputs.

C. Drift Test Results in Matched Mode

Next, we tested the long-term drift of the gyroscope under mode matched conditions. We manually matched the modes
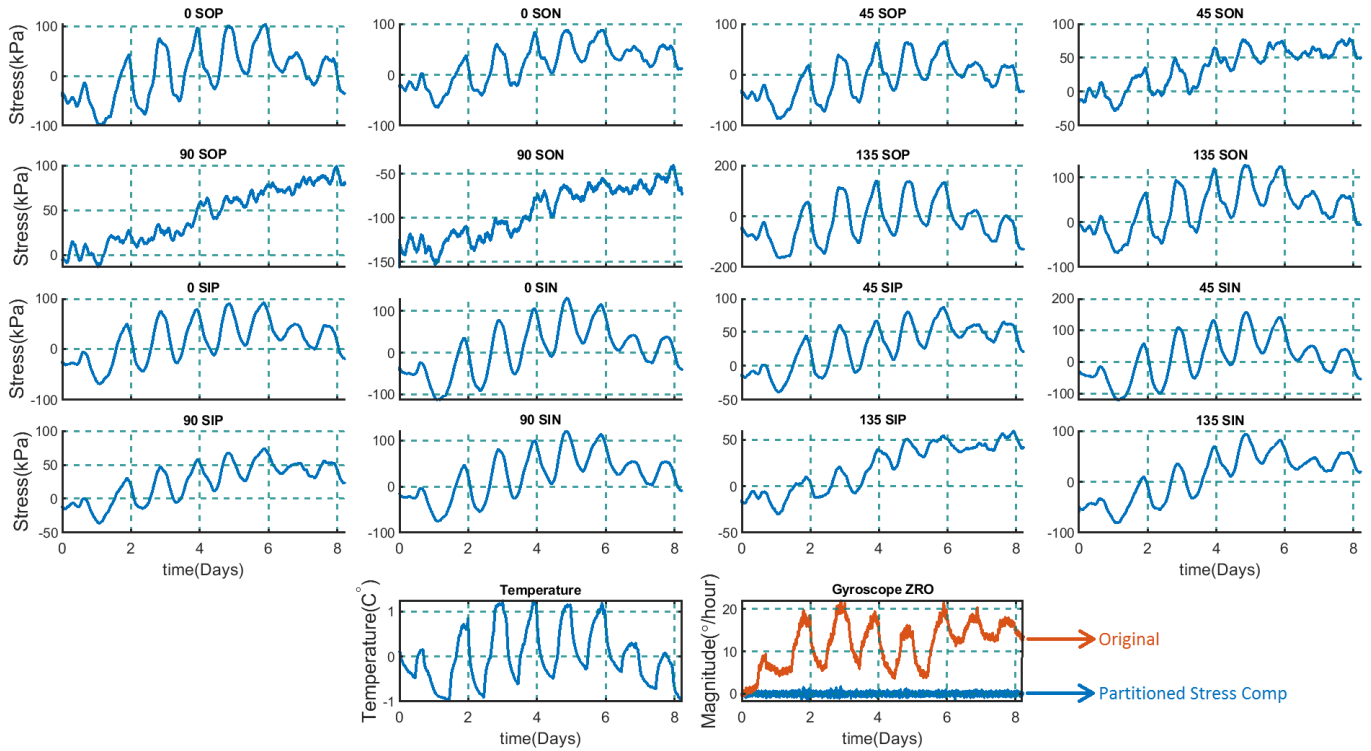
Fig. 10. The time domain plot of the 16 stress sensors, the temperature sensor and ZRO of the gyroscope in matched frequency operation for 8 days. The variations over time are plotted, refer to Fig.1.a for stress sensor locations.

by adjusting the frequency tuning voltage, and recorded the gyroscope, stress sensor, and temperature sensor outputs for 8 days. Figure 10 shows the time domain plots for 16 stress sensors, temperature, original and compensated gyroscope output. There is no active mode matching loop, and the gyroscope is operated with open-loop sense mode. The temperature changed +/-1°C during the test. It can be seen that the source of the stress changes is the temperature fluctuations. Increasing temperature leads to tensile stress and the maximum stress variation <400kPa, is less than the mismatced mode test. This can be attributed to smaller temperature changes compared to the mismatched mode test. The drift at the uncompensated gyroscope output is limited to 20°/h, thanks to the circular symmetry and matching between the drive and sense modes. Similar to the mismatched drift test, Figure 11 presents the Allan Variance for different cases. The uncompensated ARW and bias instability are $0.058°/\sqrt{h}$ and 0.3°/h, respectively. Measured ARW is 3X above the Brownian noise limit ($0.02°/\sqrt{h}$). As drive and sense modes are matched, the rate equivalent noise rises faster than the rate sensitivity, and we will investigate this issue. Temperature compensation improves the long-term drift at short averaging times and stress and temperature compensation improves the long-term drift by 4X. Partitioning the data into 12-hour intervals and calculating the individual coefficients just using the stress sensors results in 0.003 °/h stability at 2 days of averaging time and removes the long-term drift completely. On the other hand, partitioned temperature compensation provides 80X worse stability. There are inevitable frequency drift mismatches in between the drive and sense modes without an active matching loop, and
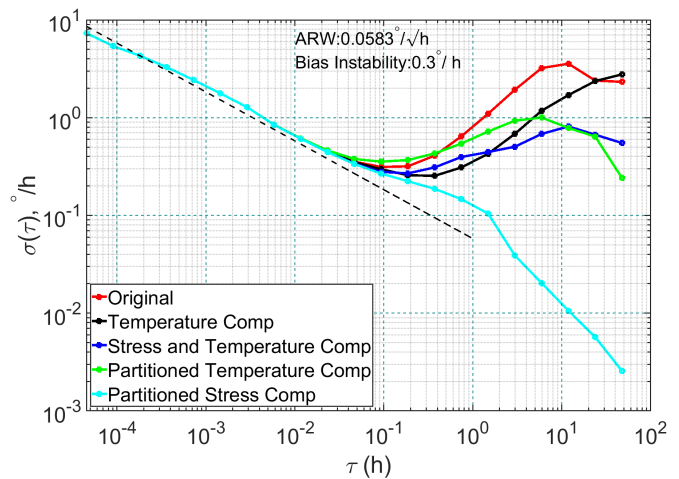

Fig. 11. The Allan deviation plots of the gyroscope output in matched frequency operation for 8 days for various compensation cases.

we believe that stress sensors capture these mismatches and correct the gyroscope output.

Long-term stress measurements both in the matched and mismatched tests indicate that the die stress is not exactly uniform across the die. There are slight differences between the stress sensors, and we think that measurement of the differences leads to performance improvement. One fundamental aspect of our work is investigating the minimum number of stress sensors needed for stress compensation. In terms of die size, if the long-term drift can be suppressed only with the
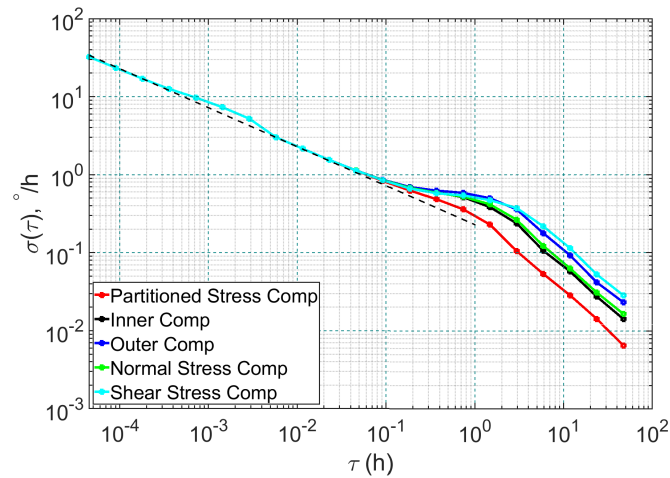
Fig. 12.   The Allan deviation plots for the mismatched operation compensated with various stress sensor sets.

Fig. 13.   The Allan deviation plots for the mismatched operation compensated with different partition periods.

internal 8 stress sensors, then stress sensors do not increase the die size for a circular gyroscope. In Figure 12 four different sets of stress sensors were used for the compensation. Each group employs 8 stress sensors and the grouping is as follows;

Inner Comp: Stress Sensors inside the ring.

Outer Comp: Stress Sensors outside the ring.

Normal Stress Comp: Stress Sensors on the x and y axis.

Shear Stress Comp: Stress Sensors on the 45° and 135° axis.

Our findings indicate that the best compensation is achieved with all the 16 stress sensors, labeled as "Partitioned Stress Comp". Using the inner stress sensors yields 2X worse stability, and using the outer stress sensors yields 4X worse stability. Just using the normal and shear sensors results in a similar performance to inner and outer stress sensor compensation, respectively. It is not straightforward to draw conclusions within the 8 stress sensor compensation, but utilizing 16 stress sensors performs the best. The analysis shows the importance of distributed stress measurement, higher stress resolution is obtained with more stress sensors leading to higher stability. The long-term drift can also be removed with just the internal stress sensors, if the die size is constraint.

We analyzed the effect of the length of partitioning on the performance. We divided the data to 12h, 24h, and 48h intervals, calculated the individual compensation coefficients for each period then assembled the data for Allan Variance analysis. Figure 13 presents the Allan Variance results for different time intervals. As the length of the partitioning increases, the Allan Variance performance gets worse. But even for 48h intervals, there is still no long-term drift. These findings align with the idea that stress to gyroscope output relation is linear in the relatively shorter time periods, but the relation itself is not linear time-invariant.

Since the mismatched mode drift test (16 days) is longer than the matched mode drift test (8 days), the analysis in Figure 12 and Figure 13 are performed for the mismatched mode drift test. Similar results would be obtained for the matched mode drift test.
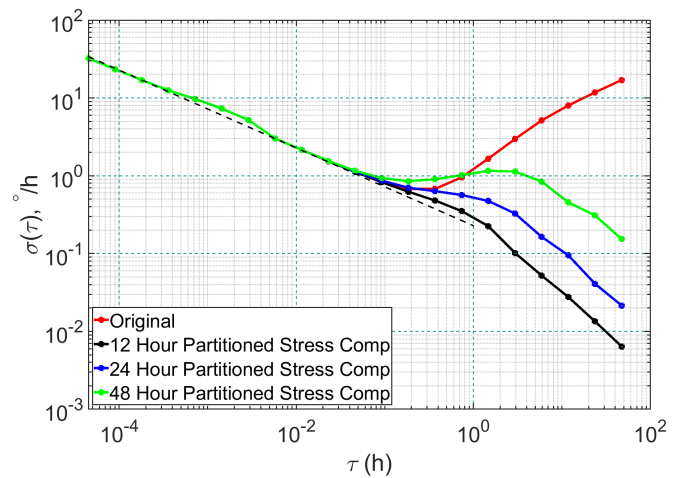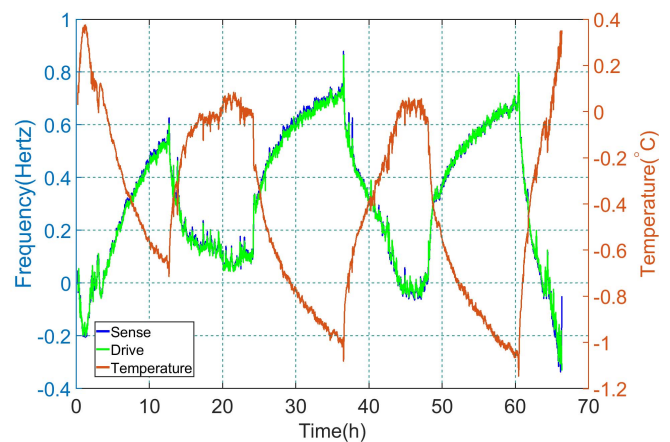

Fig. 14.   The time domain plots for the drive and sense frequency shifts and temperature changes for 65 hours.

D. Resonance Frequency Vs. Temperature Tests

Investigating the drive and sense resonance frequencies under temperature and stress changes would provide fundamental knowledge about the gyroscope drift. We continuously monitored the drive and sense resonance frequencies of our gyroscope by sequentially locking a PLL to the drive and sense modes. With a Python controlled test setup, we locked into the drive frequency for 3 minutes and then locked to the sense frequency for 3 minutes and repeated this sequence for 65 hours. Figure 14 presents the frequency shifts for the drive and sense modes, and room temperature fluctuations over time. The drive and sense frequencies closely follow each other thanks to the circular symmetry. Figure 15 shows the temperature vs drive frequency change. Although the relation is linear, a significant amount of hysteresis can be observed. The plot is colored with respect to progressing time, the frequency-temperature relation is linear for short periods, but the hysteresis manifests itself as the time progresses. Young's Modulus of silicon has -60ppm/K [35] temperature dependence, which is almost independent of doping level [36]. The temperature dependence
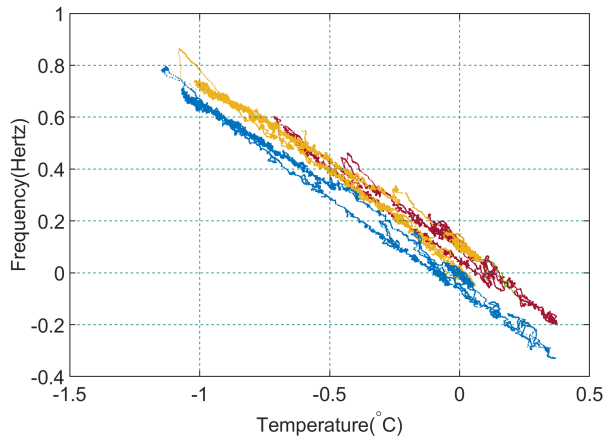
Fig. 15. The change of drive frequency vs the change of temperature, hysteresis is visible. The plot is colored with progressing time.
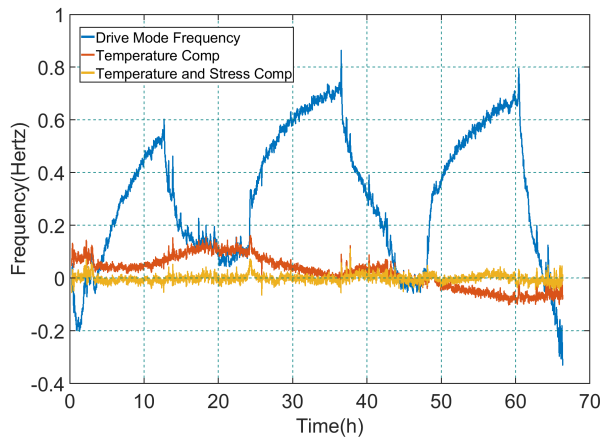

Fig. 16. Original and compensated drive frequency with temperature and stress.

leads to −30ppm/K frequency change with temperature. The temperature coefficient of frequency (TCF) in our tests is −11.6ppm/K based on Figure 15 and $f_{res} = 57.355$kHz. In order to understand the root-cause of the TCF, we reduced the proof mass high voltage to 20V from 50V and obtained a TCF of −12ppm/K. Based on these tests, the deviation of TCF from −30ppm/K is not due to electrostatics and can be attributed to the mechanical stress on the structure. The hysteresis of the frequency-temperature curve is caused by the non-repeatable stress on the suspension of the gyroscope.

Similar to the ZRO tests, we compensated the frequency with temperature and with both temperature and stress by using the least-squares method. Figure 16 shows the uncompensated, temperature compensated, and temperature and stress compensated drive frequency. There is no partial compensation, the fits are performed on the entire data set. The temperature compensation removes the frequency changes to the first order, but there are residues due to the hysteresis. Stress and temperature compensation fits to the frequency better, and the residuals are close to zero. The reported frequency tests prove that only temperature cannot explain the frequency changes. The changes can be comprehensively described with stress and temperature. The drive and sense frequencies are one of the primary metrics for the gyroscope drift. The stress compensation captures the frequency changes explaining one of the reasons for the efficiency of the drift suppression with stress compensation.

V. CONCLUSION

We reported a MEMS vibrating ring gyroscope with integrated capacitive stress sensors for the first time in this paper. The circular structure enabled the tight integration of the stress sensors with the gyroscope anchors, which we believe are responsible for the long-term drift. We have employed a bridge-type capacitive stress sensor instead of a piezoresistive stress sensor due to its compact size and temperature insensitivity. We evenly distributed 16 stress sensors across the device with 8 inside and 8 outside sensors. Testing the stress sensors on a stress test-bed showed the functionality of the stress sensors. Extensive long-term testing, 16 days in the mismatched condition and 8 days in the matched condition at room temperature, revealed the strong correlation between the stress sensor outputs and the gyroscope drift. Our initial findings indicate that the gyroscope ZRO-stress relation is linear for shorter periods of time (∼2 days), but the relationship is not entirely linear for extended time periods. Linear time-variant or nonlinear relationship lead to time varying compensation coefficients. Even though we have not discovered the gyroscope ZRO stress relation in this study, we demonstrated the ultimate stress calibration results. The gyroscope stability reaches to 0.008 °/h in mismatched operation and 0.003 °/h in matched operation at an averaging time of 2 days with no signs of drift with time partitioned stress compensation. We obtained these results from a relatively small 3.2mm outer diameter ring, thanks to the power of averaging. The analysis of the drive and sense frequencies illustrated the consistent matching between the modes, and the frequency changes can be coherently understood with the stress and temperature.

Based on the findings of this study, we believe that the stress compensation has the potential to address one of the major problems of the MEMS gyroscopes, the drift. The next steps of our research will be working on the more complex fitting algorithms to find the gyroscope ZRO-stress relation, investigating the stress compensation under extended temperature ranges, and looking into sensitivity calibration with stress. We should point out that the drift of the stress sensors could preclude an effective algorithm. We will research to reduce the drift of the stress sensors. As the first attempt, we will try differential reading and single-ended clocking, the stress sensor outputs are read single-ended with differential clocking in this study.

REFERENCES

[1] D. M. Rozelle, "The hemispherical resonator gyro: From wineglass to the planets," *Adv. Astron. Sci.*, vol. 134, pp. 1157–1178, Feb. 2009.
[2] C. H. Ahn *et al.*, "Mode-matching of wineglass mode disk resonator gyroscope in (100) single crystal silicon," *IEEE J. Microelectromech. Syst.*, vol. 24, no. 2, pp. 343–350, Apr. 2015.
[3] A. D. Challoner, H. H. Ge, and J. Y. Liu, "Boeing disc resonator gyroscope," in *Proc. IEEE/ION Position, Location Navigat. Symp. (PLANS)*, Monterey, CA, USA, May 2014, pp. 504–514.

[4] Y. Xu *et al.*, "0.015 degree-per-hour honeycomb disk resonator gyroscope," *IEEE Sensors J.*, vol. 21, no. 6, pp. 7326–7338, Mar. 2021.

[5] M. W. Putty, "A micromachined vibrating ring gyroscope," Ph.D. dissertation, Dept. Elect. Eng., Univ. Michigan, Ann Arbor, MI, USA, 1995.

[6] *High Performance MEMS Gyroscope CRS39A Series Technical Datasheet*, Silicon Sensing, Plymouth, U.K., 2021.

[7] J. Y. Cho, S. Singh, J. K. Woo, G. He, and K. Najafi, "0.00016 deg/√(hr) angle random walk (ARW) and 0.0014 deg/hr bias instability (BI) from a 5.2M-Q and 1-cm precision shell integrating (PSI) gyroscope," in *Proc. IEEE Int. Symp. Inertial Sensors Syst. (INERTIAL)*, Hiroshima, Japan, Mar. 2020, pp. 1–4.

[8] M. Gadola, A. Buffoli, M. Sansa, A. Berthelot, P. Robert, and G. Langfelder, "1.3 mm^2 Nav-grade NEMS-based gyroscope," *J. Microelectromech. Syst.*, vol. 30, no. 4, pp. 513–520, Aug. 2021.

[9] N. Vercier, B. Chaumet, B. Leverrier, and S. Bouyat, "A new silicon axisymmetric gyroscope for aerospace applications," in *Proc. DGON Inertial Sensors Syst. (ISS)*, Braunschweig, Germany, Sep. 2020, pp. 1–18.

[10] D. Endean *et al.*, "Near-navigation grade tuning fork MEMS gyroscope," in *Proc. IEEE Int. Symp. Inertial Sensors Syst.*, Naples, FL, USA, Apr. 2019, pp. 1–4.

[11] *IEEE Standard for Inertial Sensor Terminology*, IEEE Standard 528-2019 (Revision of IEEE Std 528-2001), 2019.

[12] E. Tatar, "On-chip compensation of stress, temperature, and nonlinearity in a MEMS gyroscope," Ph.D. dissertation, Dept. Elect. Comput. Eng., Carnegie Mellon Univ., Pittsburgh, PA, USA, Feb. 2016.

[13] *ADIS16488A Datasheet and Product Info | Analog Devices*, Analog Devices, Norwood, MA, USA, 2018.

[14] R. L. Kubena, R. J. Joyce, and A. D. Challoner, "Correlation of frequency, temperature, and bias stability of a Si ring gyro," in *Proc. IEEE Int. Symp. Inertial Sensors Syst. (INERTIAL)*, Laguna Beach, CA, USA, Mar. 2016, pp. 21–24.

[15] H. Ge and R. T. M'Closkey, "Simultaneous angular rate estimates extracted from a single axisymmetric resonator," *IEEE Sensors J.*, vol. 17, no. 22, pp. 7460–7469, Nov. 2017.

[16] E. Tatar, T. Mukherjee, and G. K. Fedder, "Simulation of stress effects on mode-matched MEMS gyroscope bias and scale factor," in *Proc. IEEE/ION Position, Location Navigat. Symp. (PLANS)*, Monterey, CA, USA, May 2014, pp. 16–20.

[17] X. Zhang, S. Park, and M. W. Judy, "Accurate assessment of packaging stress effects on MEMS sensors by measurement and sensor-package interaction simulations," *J. Microelectromech. Syst.*, vol. 16, no. 3, pp. 639–649, Jun. 2007.

[18] G. S. Matijasevic, C. Y. Wang, and C. C. Lee, "Thermal stress considerations in die-attachment," in *Thermal Stresses and Strain in Microelectronics Packaging*. New York, NY, USA: Springer-Verlag, 1993, pp. 194–220.

[19] E. Tatar, T. Mukherjee, and G. K. Fedder, "Stress effects and compensation of bias drift in a MEMS vibratory-rate gyroscope," *J. Microelectromech. Syst.*, vol. 26, no. 3, pp. 569–579, Jun. 2017.

[20] S. S. Kumar and B. D. Pant, "Design principles and considerations for the 'ideal' silicon piezoresistive pressure sensor: A focused review," *Microsyst. Technol.*, vol. 20, no. 7, pp. 1213–1247, May 2014.

[21] J. C. Suhling and R. C. Jaeger, "Silicon piezoresistive stress sensors and their application in electronic packaging," *IEEE Sensors J.*, vol. 1, no. 1, pp. 14–30, Jun. 2001.

[22] R. C. Jaeger, J. C. Suhling, and R. Ramani, "Errors associated with the design, calibration and application of piezoresistive stress sensors in (100) silicon," *IEEE Trans. Compon., Packag., Manuf. Technol. B*, vol. 17, no. 1, pp. 97–107, Feb. 1994.

[23] L. L. Chu, L. Que, and Y. B. Gianchandani, "Measurements of material properties using differential capacitive strain sensors," *J. Microelectromech. Syst.*, vol. 11, no. 5, pp. 489–498, Oct. 2002.

[24] M. Suster, J. Guo, N. Chaimanonart, W. H. Ko, and D. J. Young, "A high-performance MEMS capacitive strain sensing system," *J. Microelectromech. Syst.*, vol. 15, no. 5, pp. 1069–1077, Oct. 2006.

[25] H.-W. Ma, S.-M. Yao, L.-Q. Wang, and Z. Zhong, "Analysis of the displacement amplification ratio of bridge-type flexure Hinge," *Sens. Actuators A, Phys.*, vol. 132, no. 2, pp. 730–736, Nov. 2006.

[26] E. Tatar, T. Mukherjee, and G. K. Fedder, "On-chip stress compensation on the ZRO of a mode-matched MEMS gyroscope," in *Proc. IEEE Int. Symp. Inertial Sensors Syst. (INERTIAL)*, Laguna Beach, CA, USA, Mar. 2016, pp. 128–131.

[27] M. Hosseini-Pishrobat and E. Tatar, "Modeling and analysis of a MEMS vibrating ring gyroscope subject to imperfections," *J. Microelectromech. Syst.*, vol. 31, no. 4, pp. 546–560, Aug. 2022.

[28] J. Kirkhope, "In-plane vibration of a thick circular ring," *J. Sound Vibrat.*, vol. 50, no. 2, pp. 219–227, Jan. 1977.

[29] S. W. Yoon, S. Lee, and K. Najafi, "Vibration sensitivity analysis of MEMS vibratory ring gyroscopes," *Sens. Actuators A, Phys.*, vol. 171, no. 2, pp. 163–177, Nov. 2011.

[30] D. E. Serrano *et al.*, "Substrate-decoupled, bulk-acoustic wave gyroscopes: Design and evaluation of next-generation environmentally robust devices," *Microsyst. Nanoeng.*, vol. 2, no. 1, pp. 1–10, Apr. 2016.

[31] A. Efimovskaya, D. Wang, Y.-W. Lin, and A. M. Shkel, "On ordering of fundamental wineglass modes in toroidal ring gyroscope," in *Proc. IEEE SENSORS*, Oct. 2016, pp. 1–3.

[32] M. M. Torunbalci, S. E. Alper, and T. Akin, "Advanced MEMS process for wafer level hermetic encapsulation of MEMS devices using SOI cap wafers with vertical feedthroughs," *J. Microelectromech. Syst.*, vol. 24, no. 3, pp. 556–564, Jun. 2015.

[33] *HF2LI 50 MHz Lock-in Amplifier*, Zurich Instrum., Zürich, Switzerland, 2022.

[34] E. Tatar, S. E. Alper, and T. Akin, "Quadrature-error compensation and corresponding effects on the performance of fully decoupled MEMS gyroscopes," *J. Microelectromech. Syst.*, vol. 21, no. 3, pp. 656–667, Jun. 2012.

[35] M. A. Hopcroft, W. D. Nix, and T. W. Kenny, "What is the young's modulus of silicon?" *J. Microelectromech. Syst.*, vol. 19, no. 2, pp. 229–238, Apr. 2010.

[36] C. Bourgeois, E. Steinsland, N. Blanc, and N. F. de Rooij, "Design of resonators for the determination of the temperature coefficients of elastic constants of monocrystalline silicon," in *Proc. Int. Freq. Control Symp.*, 1997, pp. 791–799.

Baha Erim Uzunoglu was born in Canakkale, Turkey, in 1995. He received the B.S. degree in electrical and electronics engineering from Bogazici University, Istanbul, Turkey, in 2019. He is currently pursuing the M.S. degree in electrical and electronics engineering from Bilkent University, Ankara, Turkey. He will join North Carolina State University, Raleigh, NC, USA, to pursue his Ph.D. degree in electrical and electronics engineering. His research interests include biosensors, microfluidics, analog circuit design, and MEMS sensors specifically MEMS gyroscopes.

Derin Erkan was born in Ankara, Turkey, in March 1998. He received the B.Sc. degree in electrical and electronics engineering from Bilkent University, Ankara, in 2020, where he is currently pursuing the M.Sc. degree in electrical and electronics engineering. His research interests include analog electronics and microelectromechanical sensors, with emphasis on vibratory gyroscopes, accelerometers, and acoustic sensors.

Erdinc Tatar (Member, IEEE) was born in Denizli, Turkey, in 1985. He received the B.S. and M.S. degrees (Hons.) in electrical and electronics engineering from Middle East Technical University (METU), Ankara, Turkey, and the Ph.D. degree in electrical and computer engineering from Carnegie Mellon University, Pittsburgh, PA, USA, in 2008, 2010, and 2016, respectively. He was a Graduate Research Assistant at the Micro-Electro-Mechanical Systems Research and Applications Center, METU, from 2008 to 2011, and at Carnegie Mellon University from 2012 to 2016. From 2016 to 2019, he worked as a MEMS Design Engineer responsible for the development of the high-performance gyroscopes in Analog Devices, Inc., Wilmington, MA, USA. He has been an Assistant Professor with the National Nanotechnology Research Center (UNAM), Department of Electrical and Electronics Engineering, Bilkent University, since 2019. His research interests include MEMS sensors with a specific focus on inertial and gas sensors, microfabrication and packaging technologies, and readout and control electronics for MEMS sensors.